Journal of Materials Chemistry A

PAPER

View Article Online
View Journal | View Issue

Check for updates

Cite this: J. Mater. Chem. A, 2019, 7, 27640

Guanidinium doping enabled low-temperature fabrication of high-efficiency all-inorganic $CsPbI_2Br$ perovskite solar cells†

Junjie Ma,‡[ab] Minchao Qin,‡[a] Yuhao Li,[a] Tiankai Zhang,[c] Jianbin Xu,[c] Guojia Fang *[b] and Xinhui Lu *[a]

All-inorganic perovskite $CsPbI_2Br$ usually requires a high fabrication temperature (higher than 200 °C) and suffers from an unwanted phase transition from a photo-active cubic phase to a photo-inactive orthorhombic phase. Here, we demonstrate an effective anti-solvent-free route to simultaneously stabilize the cubic phase and lower the fabrication temperature of perovskite solar cells with guanidinium (GA) cation doping. It is suggested that a trace amount of GA in the precursor could enter the substitutional sites to stabilize the cubic phase by relaxing the lattice strain and forming strong hydrogen bonds. State-of-the-art *in situ* grazing-incidence wide-angle X-ray scattering (GIWAXS) measurements reveal that GA could advance the crystallization of the cubic phase, indicating that the formation of the perovskite cubic phase experiences a lowered energy barrier with the assistance of GA, thereby resulting in a significant decrease of the fabrication temperature. An efficiency as high as 14.34% was achieved at a low fabrication temperature of 140 °C. With the help of GA, the device maintains ~94% of its initial efficiency after being stored for 1000 h.

Received 3rd October 2019
Accepted 13th November 2019

DOI: 10.1039/c9ta10899h

rsc.li/materials-a

Published on 15 November 2019. Downloaded by National Synchrotron Radiation Research on 1/9/2020 4:38:58 AM.

1. Introduction

Organic–inorganic perovskite solar cells (PSCs) have attracted tremendous attention with the rapidly increasing power conversion efficiency (PCE) of over 24% to date.[1] However, organic–inorganic PSCs suffer from stability issues, especially thermal stability, because of the relatively high volatility of commonly employed organic cations such as methylammonium (MA) and formamidinium (FA).[2–4] Hence, all-inorganic PSCs emerge as a viable solution to address the thermal stability issue by substituting the organic cations with inorganic cations, *i.e.*, Cs^+. On the other hand, the much smaller inorganic cations largely reduce the value of the tolerance factor beyond the desired cubic phase range (0.9–1).[5] For instance, the cubic phase of $CsPbI_3$, though with a suitable band gap (E_g) of 1.7 eV for photovoltaic applications, is not stable at room temperature.[6–9]

To stabilize the cubic phase of Cs-based all-inorganic PSCs, one popular way is to use $PbI_2 \cdot x$DMAI (x = 1.1 to 1.2; DMAI, dimethylammonium iodide) as the precursor additive, which remarkably pushed the PCE of $CsPbI_3$ PSCs over 18% recently.[10] Another effective route is to employ smaller halide anions, such as Br^+, which, however, further enlarges the bandgap.[11] For instance, $CsPbBr_3$ was reported to have a stable black orthorhombic phase at room temperature but a too large E_g of 2.4 eV to sufficiently absorb sunlight.[12] Therefore, mixed halide Cs-based PSCs were proposed to balance the bandgap range and the phase stability.[13] Among the reported mixed halide Cs-based PSCs, $CsPbI_2Br$ with a bandgap of 1.9 eV is one of the most extensively studied compositions with over 16% PCEs reported.[14] However, it still suffers from the unwanted phase transition from the photo-active cubic phase to the photo-inactive orthorhombic phase at room temperature. Li *et al.* found that devices based on $CsPbI_2Br$ perovskite showed a dramatically degraded photovoltaic performance after 10 min under humidity conditions. They ascribed it to the extremely unstable α-phase $CsPbI_2Br$ in a high relative humidity (RH), leading to the color change of the films.[15] Han *et al.* pointed out that pure $CsPbI_2Br$ tends to transit to the photoinactive δ-phase at room temperature, harming the light harvesting and charge transport.[16]

For most of the all-inorganic high-efficiency perovskite solar cells, a high fabrication temperature over 200 °C is often required. These energy-consuming processes are not favorable for mass production.[17,18] There are very limited approaches

[a]Department of Physics, The Chinese University of Hong Kong, Shatin 999077, Hong Kong. E-mail: xhlu@phy.cuhk.edu.hk

[b]Key Lab of Artificial Micro- and Nano-Structures of Ministry of Education of China, School of Physics and Technology, Wuhan University, Wuhan 430072, People's Republic of China. E-mail: gjfang@whu.edu.cn

[c]Department of Electronic Engineering, The Chinese University of Hong Kong, Shatin, New Territories 999077, Hong Kong

† Electronic supplementary information (ESI) available. See DOI: 10.1039/c9ta10899h

‡ J. M. and M. Q. contributed equally to this work.

This journal is © The Royal Society of Chemistry 2019

Published on 15 November 2019. Downloaded by National Synchrotron Radiation Research on 1/9/2020 4:38:58 AM.

developed so far capable of effectively lowering the fabrication temperature below 200 °C, but at the cost of PCE decrease.[42] For instance, DMSO assisted annealing treatment was developed to control the perovskite crystallization and produced $CsPbI_2Br$ PSCs with a 10.4% PCE with a fabrication temperature of 120 °C.[19] A synthesized Lewis base adduct allowed a low activation energy route to form $CsPbI_2Br$ perovskite films and achieved a PCE of 13.54% with a fabrication temperature of 120 °C.[20] Thus, the search of low-temperature fabrication strategies for all-inorganic perovskite systems is highly desirable.

In this work, we present a brand-new method to fabricate high-efficiency $CsPbI_2Br$ PSCs with enhanced phase stability at a low temperature through organic guanidinium cation ($C(NH_2)_3$), *i.e.* GA, doping. Furthermore, our method is anti-solvent free, providing another advantage for future mass production. In comparison to the MA and FA cations, GA has three symmetric amino groups that contribute to the formation of more hydrogen bonds, which play a key role in structural stabilization. The atomic-level evidence confirmed that GA could be directly incorporated into the $MAPbI_3$ and $FAPbI_3$ lattices, forming pure $GA_xMA_{1-x}PbI_3$ or $GA_xFA_{1-x}PbI_3$ phases.[21] On the other hand, unlike the bulky long-chain BA or PEA cations, GA has a moderate size to fit into the lattice without impeding the carrier transport.[22,23,44] GA cations were previously employed in the $MAPbI_3$ system to improve the material stability by partially substituting the MA organic cations.[24,43] Some theory calculations pointed out that GA can effectively stiffen the inorganic Pb–I lattice and reduce formation of defects.[25] It was reported that $(FA,Cs)Pb(I,Br)_3$ perovskites get enhanced defect tolerance and phase stability *via* GA alloying.[26] Guanidinium thiocyanate (GASCN) was introduced into Sn–Pb mixed perovskite films to improve the structural and optoelectronic properties *via* the formation of two-dimensional (2D) structures at grain boundaries.[27] It is indeed very difficult to conclude whether GA cations are inserted into the lattice or passivate grain boundaries, which may depend on the perovskite composition, fabrication method, GA additive concentration, *etc.* Here, we demonstrate that only a trace amount (~0.5 mol%) of GA could simultaneously stabilize the cubic phase and lower the fabrication temperature of all-inorganic $CsPbI_2Br$. Based on the X-ray diffraction (XRD), fourier-transform infrared spectroscopy (FTIR), and X-ray photoelectron spectroscopy (XPS) results, it is evident that GA could enter the substitutional sites of Cs to relax the lattice strain created by the small Cs cations and form strong hydrogen bonds with the neighboring $[PbI_6]^{4-}$ octahedral building blocks to suppress the phase transition from the cubic phase (α-phase) to orthorhombic phase (δ-phase) (Fig. 1a). Furthermore, state-of-the-art *in situ* grazing-incidence wide-angle X-ray scattering (GIWAXS) measurements reveal the kinetic role of GA in expediting the formation of the $CsPbI_2Br$ cubic phase. It implies that the energy barrier to form the cubic phase is significantly lowered by the incorporation of GA, thus allowing a much lower fabrication temperature. In addition, a surface treatment with GABr could further passivate the perovskite surface defects and better orient the crystals. A PCE as high as 14.34% is achieved with a fabrication temperature of 140 °C. To our knowledge, it is the

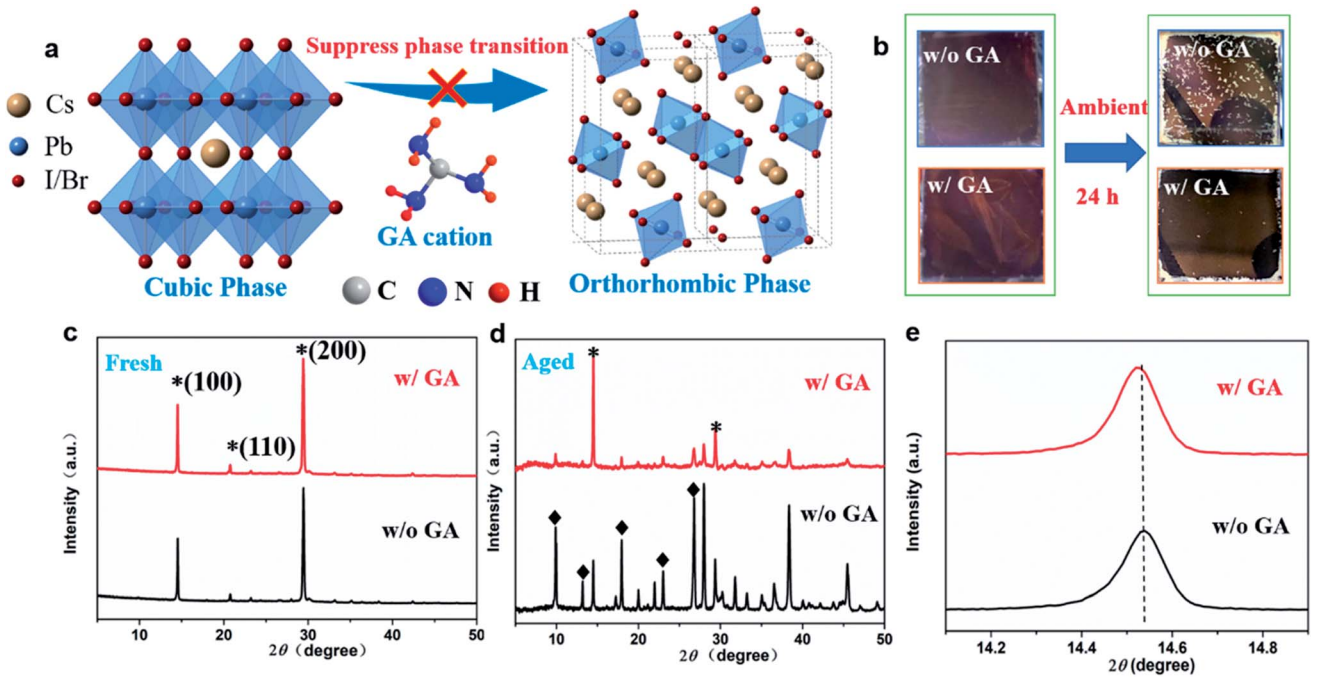

Fig. 1 (a) Schematic illustration of suppressing the phase transition *via* introducing GA cations. (b) Photographs of perovskite films with and without GA aged for 24 hours under ambient conditions with below 30% relative humidity. The corresponding XRD patterns of (c) fresh and (d) aged perovskite films with and without GA. * and ◆ denote the perovskite cubic phase and non-perovskite orthorhombic phase, respectively. (e) The XRD profiles of the (100) peak of fresh perovskite films.

Published on 15 November 2019. Downloaded by National Synchrotron Radiation Research on 1/9/2020 4:38:58 AM.

highest efficiency reported among the $CsPbI_2Br$ PSCs fabricated at a low temperature (<150 °C). Specifically, the device with GA retains 94% of its initial efficiency after being stored for 1000 h under nitrogen conditions.

2. Results and discussion

First, we demonstrate the effectiveness of GA doping in stabilizing the $CsPbI_2Br$ film. GA cations were introduced into the $CsPbI_2Br$ precursor solution by adding a trace amount (0.5 mol%) of the $GAPbI_2Br$ solution in order to maintain the perovskite stoichiometric ratio and eliminate the effect from the I/Br ratio variation. Fig. 1b shows the comparison of the $CsPbI_2Br$ films with and without GA stored in dry air for 24 hours. Apparently, the film without GA degrades severely with the appearance of a lot of color fading areas, while the film with GA shows a uniform black color. XRD measurements were carried out to identify the phase composition of the film. As shown in Fig. 1c, both fresh films exhibit three main Bragg peaks at $2\theta = 14.6°$, 20.8° and 29.3° which are indexed as the (100), (110), and (200) planes of the perovskite pseudo cubic α-phase, respectively.[28] For the aged films without GA, the XRD spectrum exhibits strong Bragg peaks of the orthorhombic δ-phase, indicating that the cubic phase of $CsPbI_2Br$ is unstable.[29] In contrast, the aged film with GA shows much less and weaker δ-phase signals, consistent with the film appearance. The XRD pattern of the pure $GAPbI_2Br$ film is included in ESI Fig. S1.† The absence of $GAPbI_2Br$ diffraction peaks in the $CsPbI_2Br$ film with GA confirms that no obvious heterogeneous phase segregation was produced by the GA doping. Furthermore, the (100) peak position shifts slightly to a lower diffraction angle, suggesting that the relatively larger GA cations enter the substitutional sites of Cs^+ causing a lattice expansion. Such a lattice expansion could compensate with the lattice distortion caused by the small Cs^+, being critical to stabilize the α-phase. Therefore, the stoichiometric solutions of $GAPbI_2Br$ used in our work are mainly aiding the thin films by inclusion into the lattice. In addition, the film crystallinity is further enhanced by adding GA in the light of decreased peak width of the (100) peak from 0.129° to 0.125° after GA doping.

FTIR measurements were performed to detect the existence of GA in the perovskite film by probing the stretching vibration of the functional groups (Fig. 2a). Compared to the film without GA, the film with GA exhibits three vibrational peaks located at 1640, 1410 and 1315 cm^{-1}, corresponding to the vibration of N–H, C–N, and C–H bonds, signifying the existence of the organic GA cations in the film.[30] These functional group peaks are consistent with those detected from the pure $GAPbI_2Br$ (Fig. S2†). XPS measurements were carried out in the N 1s, I 3d and Br 3d regions (Fig. 2b–d) to further confirm the presence of GA and to understand its interaction with halide atoms. An N 1s signal was detected in the film with GA, but not in the film without GA, as expected. All the spin–orbital doublet peaks of I ($3d_{3/2}$ and $3d_{5/2}$) and Br ($3d_{3/2}$ and $3d_{5/2}$) shift slightly to stronger binding energy with the addition of GA. We attribute this to the hydrogen bonds formed between the three amino groups of GA

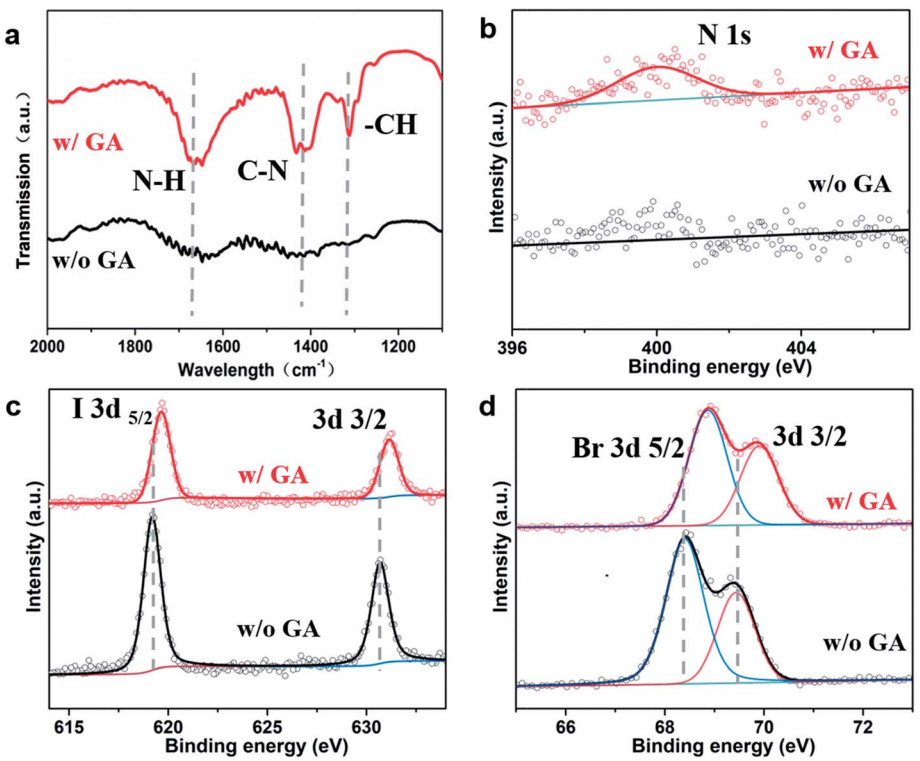

Fig. 2 (a) FTIR spectra of $CsPbI_2Br$ films with and without GA. The XPS spectra of (b) N 1s, (c) I 3d, and (d) Br 3d in the $CsPbI_2Br$ films with and without GA.

 This journal is © The Royal Society of Chemistry 2019

Published on 15 November 2019. Downloaded by National Synchrotron Radiation Research on 1/9/2020 4:38:58 AM.

and halide anions. It was reported that the positively charged (δ^+) ammonium H atom and negatively charged (δ^-) halide atom tend to form hydrogen bonds, such as N–$H^+\cdots I^-$ and N–$H^+\cdots Br^-$.[24,31–33] The incorporation of GA increases the number of H bonds compared with the small Cs cation, thus reducing the H–I or H–Br distance and inducing the XPS peak shift.[43] The corresponding schematic of hydrogen bonding interaction between GA^+ and the lead-halide framework is illustrated in Fig. S3.†

In situ grazing-incidence wide-angle X-ray scattering (GIWAXS) was employed to investigate the role of GA in the $CsPbI_2Br$ crystallization process during spin coating. The measurements were performed with an incidence angle of 2°. The peak located at $q_z = 1.85$ Å^{-1} originates from the substrate, implying the full penetration of the source beam to probe the bulk structure of the film.[34] Fig. 3a and d present the intensity profiles along the q_z direction for the $CsPbI_2Br$ films without and with GA, accompanied by the false-color intensity maps *versus* q_z and frame numbers (3 s per frame) in Fig. 3b and e. The corresponding time evolution of the area of the scattering peaks at $q_z = 1.04$ Å^{-1} and 0.72 Å^{-1} is shown in Fig. 3c and f to signify the overall crystallinity of the black α-phase and yellow δ-phase, respectively. The whole process can be divided into three stages: (I) the solution stage; (II) the crystal growth stage; (III) the crystallinity saturation stage. For the film without GA (Fig. 3b), stage II begins at the ~60th frame with three scattering peaks appearing at $q_z = 1.04$, 1.45 and 2.06 Å^{-1}, which are indexed to the (100), (110), and (200) planes of the cubic phase respectively and lasts for ~25 frames (~75 s) before saturation. The yellow δ-phase emerges in stage III, indicated by the appearance of a tiny scattering peak at $q_z = 0.72$ Å^{-1}. Remarkably, the addition of GA could give rise to a much earlier initiation of the perovskite crystallization at the ~30th frame (Fig. 3e). Besides, it takes much shorter time (~10 frames/30 s) to reach the comparable crystallinity, compared with the film without GA. The film remains in the pure α-phase without the unwanted phase transition to δ-phase in stage III. The (100) peak area of the film with GA is also larger than that without GA, suggesting that the

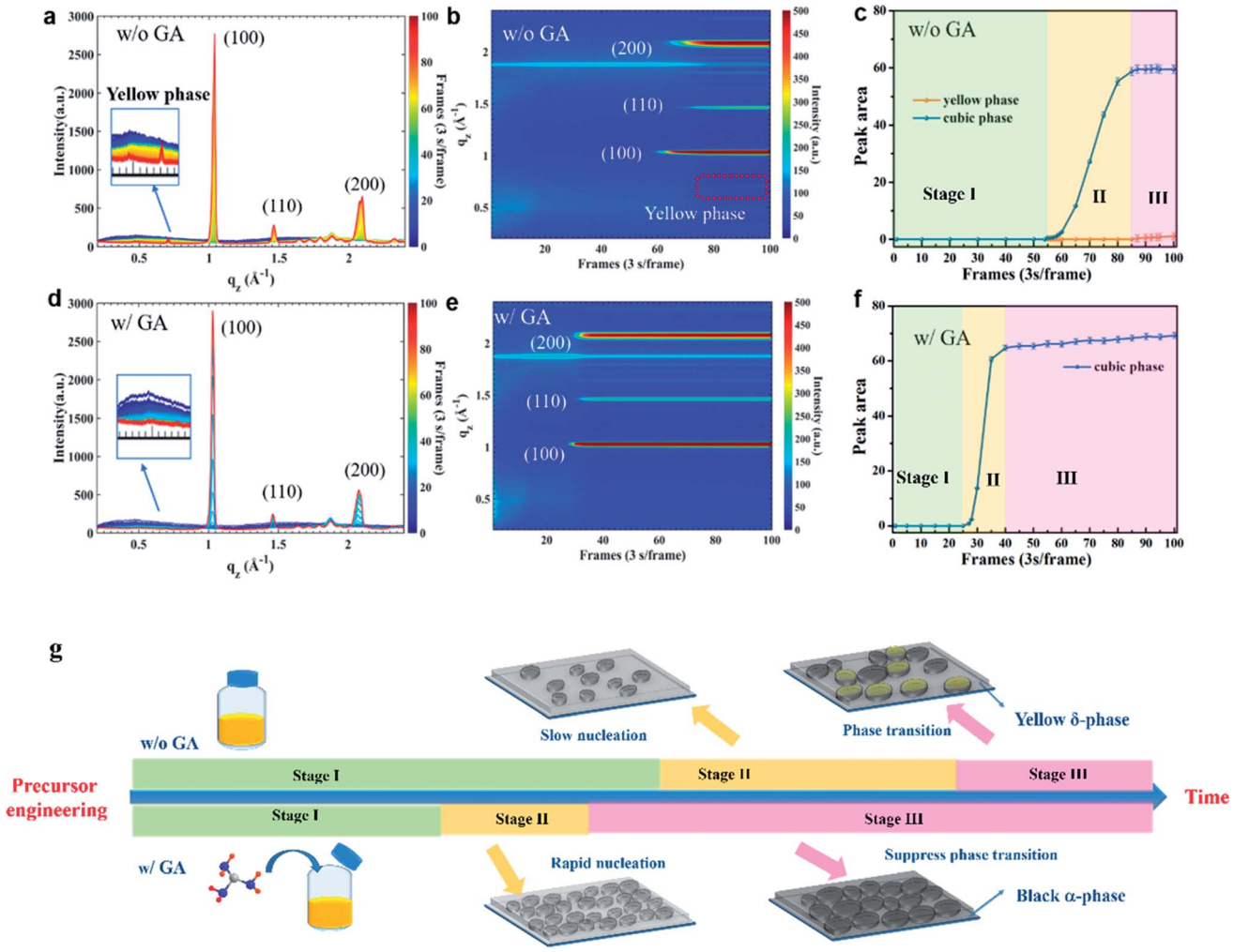

Fig. 3 The intensity profiles along the q_z direction for the $CsPbI_2Br$ films (a) without and (d) with GA from *in situ* GIWAXS measurements. False-color intensity maps *versus* q_z and the frame numbers for the $CsPbI_2Br$ films (b) without and (e) with GA. The peak areas of the cubic (100) phase and yellow phase as a function of the frame numbers for the corresponding films (c) without and (f) with GA. (g) A schematic diagram of the crystallization of $CsPbI_2Br$ without and with GA.

Published on 15 November 2019. Downloaded by National Synchrotron Radiation Research on 1/9/2020 4:38:58 AM.

incorporation of GA could enhance the overall crystallinity of the α-phase. Together, it is suggested that GA could advance and strengthen the $CsPbI_2Br$ cubic phase and suppress the phase transition to the yellow phase. The corresponding schematic of the crystallization process is illustrated in Fig. 3g.

A facile low-temperature process without the antisolvent procedure was developed to fabricate high quality $CsPbI_2Br$ films. As illustrated in Fig. 4a, the spin-coated film was annealed at a low temperature of 40 °C for 1 min and a high temperature of 140 °C for 10 min. Subsequently, the film was treated with the GABr solution to passivate the surface by inducing a secondary crystal growth without introducing foreign ions.[35] The resulted film was very smooth and mirror-like. Fig. 4c shows a photo of the 25 cm^2 mirror-like perovskite film produced with this process to demonstrate its capability in large-scale device fabrication. The ultraviolet-visible absorption (UV-vis) and photoluminescence (PL) spectra were measured to study the optical properties of the $CsPbI_2Br$ films (Fig. 4d). The absorption of the pure $GAPbI_2Br$ film is shown in Fig. S4† as a reference. For all the films, the optical bandgap estimated from the absorption edge is ~1.9 eV (~642 nm), in agreement with the theoretical bandgap of $CsPbI_2Br$.[13] It suggests that doping with GA in the precursor solution and through the surface passivation has negligible effects on the optical bandgap, which is also supported by the unchanged PL peak position at 642 nm. On the other hand, both treatments could give rise to a certain degree of PL quenching for the perovskite film coated on the ZnO electron transporting layer (ETL), demonstrating their influence on promoting the charge collection.[36,37]

To correlate the effects of GA doping with the device performance, we fabricated solar cells with a device structure of ITO/ZnO/perovskite (~500 nm)/Spiro-OMeTAD/Au. Fig. 4b shows a cross-sectional scanning electron microscopy (SEM) image of a typical device. The champion current density–voltage (*J*–*V*) curves of the devices based on the perovskite film without or with GA in the precursor solution and with GA in both the precursor and passivation are plotted in Fig. 4e. The detailed device characteristics are summarized in Table 1. The best PCE of 14.34% was achieved for the film with GA and passivation,

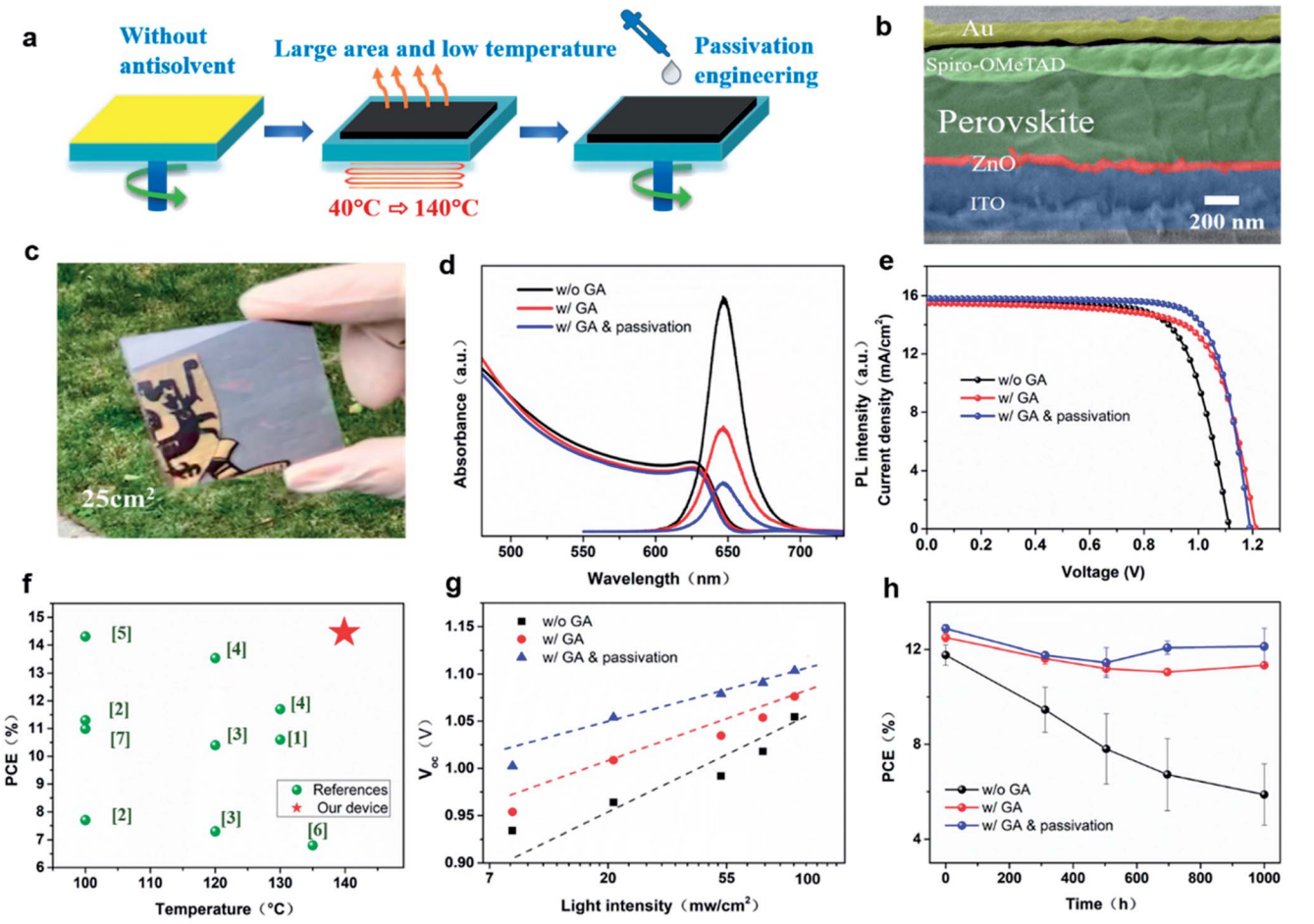

Fig. 4 (a) Schematic view of the $CsPbI_2Br$ film fabrication process. (b) The cross-sectional SEM image of a typical integrated device. (c) The photograph of the 25 cm^2 $CsPbI_2Br$ film. (d) UV-vis and PL spectra of the corresponding $CsPbI_2Br$ films deposited on the ZnO ETL. (e) *J*–*V* curves of the champion devices based on different $CsPbI_2Br$ films (without GA, with GA, and with GA & passivation). (f) A PCE summary of previously reported $CsPbI_2Br$ PSCs fabricated at low temperatures (<150 °C). (g) The V_{oc} as a function of the light intensity for the corresponding devices. (h) Long-term stability test.

 This journal is © The Royal Society of Chemistry 2019

Published on 15 November 2019. Downloaded by National Synchrotron Radiation Research on 1/9/2020 4:38:58 AM.

Table 1 The champion photovoltaic parameters of the PSCs based on the perovskite film without GA, with GA, and with GA and passivation

Devices	V_{oc} (V)	J_{sc} (mA cm^{-2})	FF (%)	PCE (%)
w/o GA	1.11	15.74	71.16	12.48
w/GA	1.21	15.49	71.15	13.34
w/GA & passivation	1.19	15.80	76.21	14.34

showing an open-circuit voltage V_{oc} of 1.19 V, a short-circuit current density J_{sc} of 15.8 mA cm^{-2} and a fill-factor FF of 76.21%. The statistics of device parameters are shown in Fig. S5 and Table S1.† Compared with the control devices, the GA doped devices demonstrate enhanced V_{oc} and FF, indicating that the incorporation of GA could reduce the charge recombination.[38] The annealing temperature is also optimized (Fig. S6 and Table S2†). We reviewed previously reported PCEs of low-temperature-fabricated $CsPbI_2Br$ PSCs (Table S3†), as presented in Fig. 4f. It indicates that our result is among the best in this catalog.[13,39] The corresponding references for the reference points are shown in the ESI.†

The charge recombination mechanism of the corresponding films was investigated by the light intensity dependence of V_{oc}, as shown in Fig. 4g. We calculated the ideality factor n from the formula $V_{oc} = n\left(\frac{k_B T}{q}\right)\ln I + \text{const}$, where k_B is the Boltzmann constant, T is the temperature, q is the electric charge and I is the light intensity.[18] We found that the film without GA shows an n of 2.52, while the n of the films with GA and with GA & passivation is 1.87 and 1.75, respectively. The smaller value of n implies that trap-assisted Shockley-Read-Hall (SRH) recombination can be effectively suppressed by doping with GA in the precursor and surface passivation, in agreement with the observed increase in V_{oc} and FF.[40]

A series of photographs of the $CsPbI_2Br$ films with and without GA for different amounts of time durations under ambient conditions with around 50% relative humidity are shown in Fig. S7.† It is obvious that the $CsPbI_2Br$ film with GA

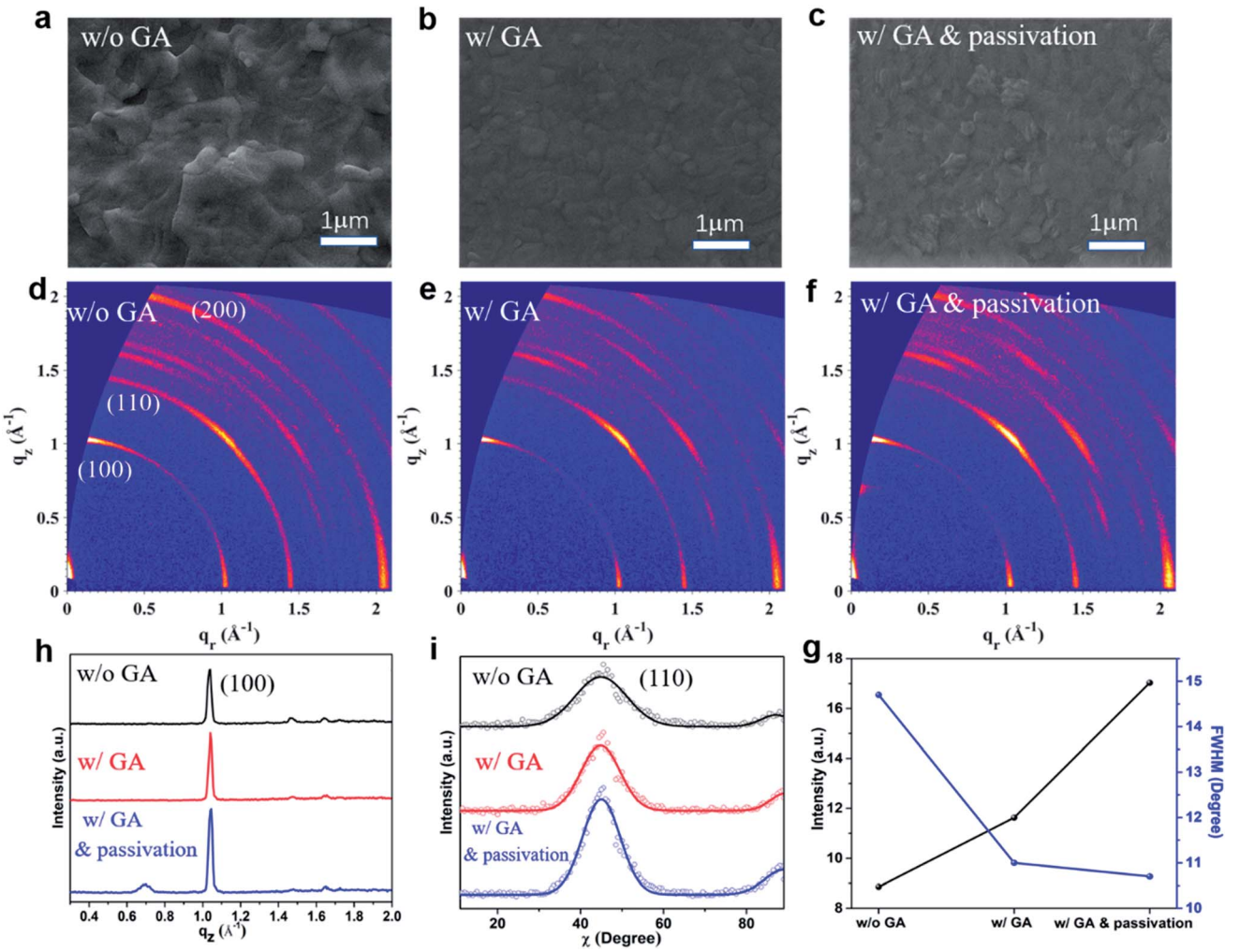

Fig. 5 (a–c) Top-view SEM images and (d–f) GIWAXS patterns of the $CsPbI_2Br$ films without GA, with GA, and with GA & passivation, respectively. (h) The GIWAXS intensity profiles along the q_z direction of the corresponding films. (i) The polar intensity profiles along the (110) plane in the q_r range of 1.4 to 1.5 Å^{-1}, and (g) the peak intensity and FWHM of the corresponding films.

Published on 15 November 2019. Downloaded by National Synchrotron Radiation Research on 1/9/2020 4:38:58 AM.

experiences much slower degradation than the control film without GA. The long-term stability of the devices was examined by storing them in a glovebox for 1000 hours. As shown in Fig. 4h, the device without GA degraded quickly. With the help of GA, the devices retained ~94% of their initial PCE. We attribute the enhanced long-term stability to the phase stability enhanced by the incorporation of GA into the cubic phase lattice.

The surface and bulk morphology of the $CsPbI_2Br$ films without GA, with GA, and with GA & passivation was further studied by SEM and GIWAXS measurements. In Fig. 5a, the film without GA has a rough surface with inhomogeneous crystal domains. In contrast, the films with GA (Fig. 5b) show uniformly packed crystalline grains. Fig. 5d–f present the two-dimensional (2D) GIWAXS patterns of the films. And the corresponding intensity profiles in the q_z direction and the polar angle (χ) along the (110) ring are shown in Fig. 5h and i, respectively. All the films exhibit clear perovskite cubic phase scattering peaks with the (100) plane preferentially oriented in the out-of-plane direction, indicating that our annealing process could promote the stacking of the corner-sharing $[PbI_6]^{4-}$ octahedra in the vertical direction, being beneficial for the charge transport.[27] The crystallinity and orientational order could be further enhanced by adding GA in the precursor solution and surface passivation (Fig. 5i and g), manifested by the increase of the scattering intensity and the narrowing polar angle peak width. The better morphology, crystallinity and orientational order of the perovskite film with GA could be the main reason for the overall V_{oc} and FF enhancement. It is worth noting that a tiny peak at $q_z = 0.7$ Å^{-1} appeared in the film with GA & passivation. It is assigned to the formation of 1D $GAPbI_2Br$ due to the surface passivation process.[41] The SEM and 2D GIWAXS results of the pure $GAPbI_2Br$ film are shown in Fig. S8.† $GAPbI_2Br$ shows a rod-like morphology, which might explain the enhanced orientational order of the resultant perovskite phase. The slight decrease of V_{oc} after the GABr treatment could be caused by the formation of 1D $GAPbI_2Br$ on the perovskite film surface.

3. Conclusions

In conclusion, we have demonstrated that introducing GA cations could effectively improve the structural stability and device performance of $CsPbI_2Br$ PSCs. A PCE as high as 14.34% has been achieved with an industry-friendly low-temperature and antisolvent-free fabrication process. The GA-doped device retains 94% of its initial efficiency after being stored for 1000 h under nitrogen conditions. The characterization results suggest that the incorporation of GA could promote the formation of the α-phase and increase the crystallinity and orientational order of the resultant films. The reason for this is that GA could lower the energy barrier to form the cubic phase, which is supported by the *in situ* GIWAXS results that the perovskite phase is formed much earlier with the GA doping. This is also in agreement with the fact that only a low temperature is required in the device fabrication. Hence, this work not only provides a facile way to improve the structural stability and efficiency of all-inorganic PSCs, but also uncovers the underlying mechanism of large organic cations in promoting the crystallization process of the perovskite α-phase.

Conflicts of interest

There are no conflicts to declare.

Acknowledgements

The authors are grateful for the beam time and technical support provided by 23A SWAXS and BL09A2 U5 beamlines at NSRRC, Hsinchu. The authors acknowledge the financial support from Research Grants Council of Hong Kong (RGC) (General Research Fund No. 14314216 and Theme-based Research Scheme No. T23-407/13-N) and CUHK Direct Grant (No. 4441636).

References

1 Q. Jiang, Y. Zhao, X. Zhang, X. Yang, Y. Chen, Z. Chu, Q. Ye, X. Li, Z. Yin and J. You, *Nat. Photonics*, 2019, **13**, 460–466.
2 F. Lang, O. Shargaieva, V. V. Brus, H. C. Neitzert, J. Rappich and N. H. Nickel, *Adv. Mater.*, 2018, **30**, 1702905.
3 S. Aharon, A. Dymshits, A. Rotem and L. Etgar, *J. Mater. Chem. A*, 2015, **3**, 9171–9178.
4 Q. Wang and A. Abate, *Adv. Mater. Interfaces*, 2018, **5**, 1800264.
5 Q. Tai, K.-C. Tang and F. Yan, *Energy Environ. Sci.*, 2019, **12**, 2375–2405.
6 T. Wu, Y. Wang, Z. Dai, D. Cui, T. Wang, X. Meng, E. Bi, X. Yang and L. Han, *Adv. Mater.*, 2019, **31**, e1900605.
7 K. Wang, Z. Jin, L. Liang, H. Bian, D. Bai, H. Wang, J. Zhang, Q. Wang and S. Liu, *Nat. Commun.*, 2018, **9**, 4544.
8 P. Wang, X. Zhang, Y. Zhou, Q. Jiang, Q. Ye, Z. Chu, X. Li, X. Yang, Z. Yin and J. You, *Nat. Commun.*, 2018, **9**, 2225.
9 Y. Hu, F. Bai, X. Liu, Q. Ji, X. Miao, T. Qiu and S. Zhang, *ACS Energy Lett.*, 2017, **2**, 2219–2227.
10 Y. Wang, M. I. Dar, L. K. Ono, T. Y. Zhang, M. Kan, Y. Li, L. Zhang, X. Wang, Y. G. Yang, X. Gao, Y. Qi, M. Grätzel and Y. Zhao, *Science*, 2019, **365**, 591–595.
11 H. Chen, S. Xiang, W. Li, H. Liu, L. Zhu and S. Yang, *Sol. RRL*, 2018, **2**, 1700188.
12 G. Wang, W. Dong, A. Gurung, K. Chen, F. Wu, Q. He, R. Pathak and Q. Qiao, *J. Power Sources*, 2019, **432**, 48–54.
13 Q. Zeng, X. Zhang, C. Liu, T. Feng, Z. Chen, W. Zhang, W. Zheng, H. Zhang and B. Yang, *Sol. RRL*, 2019, **3**, 1800239.
14 J. Tian, Q. Xue, X. Tang, Y. Chen, N. Li, Z. Hu, T. Shi, X. Wang, F. Huang, C. J. Brabec, H. L. Yip and Y. Cao, *Adv. Mater.*, 2019, **31**, e1901152.
15 W. Chen, H. Chen, G. Xu, R. Xue, S. Wang, Y. Li and Y. Li, *Joule*, 2019, **3**, 191–204.
16 Z. Zeng, J. Zhang, X. Gan, H. Sun, M. Shang, D. Hou, C. Lu, R. Chen, Y. Zhu and L. Han, *Adv. Energy Mater.*, 2018, **8**, 1801050.
17 D. Bai, H. Bian, Z. Jin, H. Wang, L. Meng, Q. Wang and S. Liu, *Nano Energy*, 2018, **52**, 408–415.

 This journal is © The Royal Society of Chemistry 2019

Published on 15 November 2019. Downloaded by National Synchrotron Radiation Research on 1/9/2020 4:38:58 AM.

18 G. Yin, H. Zhao, H. Jiang, S. Yuan, T. Niu, K. Zhao, Z. Liu and S. F. Liu, *Adv. Funct. Mater.*, 2018, **28**, 1803269.
19 H. Rao, S. Ye, F. Gu, Z. Zhao, Z. Liu, Z. Bian and C. Huang, *Adv. Energy Mater.*, 2018, **8**, 1800758.
20 H. Jiang, J. Feng, H. Zhao, G. Li, G. Yin, Y. Han, F. Yan, Z. Liu and S. F. Liu, *Adv. Sci.*, 2018, **5**, 1801117.
21 D. J. Kubicki, D. Prochowicz, A. Hofstetter, M. Saski, P. Yadav, D. Bi, N. Pellet, J. Lewinski, S. M. Zakeeruddin, M. Gratzel and L. Emsley, *J. Am. Chem. Soc.*, 2018, **140**, 3345–3351.
22 Y. Jiang, J. Yuan, Y. Ni, J. Yang, Y. Wang, T. Jiu, M. Yuan and J. Chen, *Joule*, 2018, **2**, 1356–1368.
23 J.-F. Liao, H.-S. Rao, B.-X. Chen, D.-B. Kuang and C.-Y. Su, *J. Mater. Chem. A*, 2017, **5**, 2066–2072.
24 A. D. Jodlowski, C. Roldán-Carmona, G. Grancini, M. Salado, M. Ralaiarisoa, S. Ahmad, N. Koch, L. Camacho, G. de Miguel and M. K. Nazeeruddin, *Nat. Energy*, 2017, **2**, 972–979.
25 J. He, W.-H. Fang, R. Long and O. V. Prezhdo, *ACS Energy Lett.*, 2018, **3**, 2070–2076.
26 R. J. Stoddard, A. Rajagopal, R. L. Palmer, I. L. Braly, A. K. Y. Jen and H. W. Hillhouse, *ACS Energy Lett.*, 2018, **3**, 1261–1268.
27 J. Tong, Z. Song, D. H. Kim, X. Chen, C. Chen, A. F. Palmstrom, P. F. Ndione, M. O. Reese, S. P. Dunfield, O. G. Reid, J. Liu, F. Zhang, S. P. Harvey, Z. Li, S. T. Christensen, G. Teeter, D. Zhao, M. M. Al-Jassim, M. F. A. M. van Hest, M. C. Beard, S. E. Shaheen, J. J. Berry, Y. Yan and K. Zhu, *Science*, 2019, **364**, 475–479.
28 L. Yan, Q. Xue, M. Liu, Z. Zhu, J. Tian, Z. Li, Z. Chen, Z. Chen, H. Yan, H.-L. Yip and Y. Cao, *Adv. Mater.*, 2018, **30**, 1802509.
29 S. Xiang, W. Li, Y. Wei, J. Liu, H. Liu, L. Zhu and H. Chen, *Nanoscale*, 2018, **10**, 9996–10004.
30 G. Giorgi, J.-I. Fujisawa, H. Segawa and K. Yamashita, *J. Phys. Chem. C*, 2015, **119**, 4694–4701.
31 X. Hou, Y. Hu, H. Liu, A. Mei, X. Li, M. Duan, G. Zhang, Y. Rong and H. Han, *J. Mater. Chem. A*, 2017, **5**, 73–78.
32 J. H. Lee, J. H. Lee, E. H. Kong and H. M. Jang, *Sci. Rep.*, 2016, **6**, 21687.
33 J. H. Lee, N. C. Bristowe, P. D. Bristowe and A. K. Cheetham, *Chem. Commun.*, 2015, **51**, 6434–6437.
34 M. Qin, K. Tse, T. K. Lau, Y. Li, C. J. Su, G. Yang, J. Chen, J. Zhu, U. S. Jeng, G. Li, H. Chen and X. Lu, *Adv. Mater.*, 2019, **31**, e1901284.
35 D. Luo, W. Yang, Z. Wang, A. Sadhanala, Q. Hu, R. Su, R. Shivanna, G. F. Trindade, J. F. Watts, Z. Xu, T. Liu, K. Chen, F. Ye, P. Wu, L. Zhao, J. Wu, Y. Tu, Y. Zhang, X. Yang, W. Zhang, R. H. Friend, Q. Gong, H. J. Snaith and R. Zhu, *Science*, 2018, **360**, 1442–1446.
36 S. Song, G. Kang, L. Pyeon, C. Lim, G.-Y. Lee, T. Park and J. Choi, *ACS Energy Lett.*, 2017, **2**, 2667–2673.
37 M. Zhang, J. Zhu, K. Liu, G. Zheng, G. Zhao, L. Li, Y. Meng, T. Guo, H. Zhou and X. Zhan, *J. Mater. Chem. A*, 2017, **5**, 24820–24825.
38 A. Zohar, M. Kulbak, I. Levine, G. Hodes, A. Kahn and D. Cahen, *ACS Energy Lett.*, 2018, **4**, 1–7.
39 H. Zai, D. Zhang, L. Li, C. Zhu, S. Ma, Y. Zhao, Z. Zhao, C. Chen, H. Zhou, Y. Li and Q. Chen, *J. Mater. Chem. A*, 2018, **6**, 23602–23609.
40 J. Shi, J. Dong, S. Lv, Y. Xu, L. Zhu, J. Xiao, X. Xu, H. Wu, D. Li, Y. Luo and Q. Meng, *Appl. Phys. Lett.*, 2014, **104**, 063901.
41 Y. Zhang, P. Wang, M. C. Tang, D. Barrit, W. Ke, J. Liu, T. Luo, Y. Liu, T. Niu, D. M. Smilgies, Z. Yang, Z. Liu, S. Jin, M. G. Kanatzidis, A. Amassian, S. F. Liu and K. Zhao, *J. Am. Chem. Soc.*, 2019, **141**, 2684–2694.
42 Y. Fu, M. T. Rea, J. Chen, D. J. Morrow, M. P. Hautzinger, Y. Zhao, D. Pan, L. H. Manger, J. C. Wright, R. H. Goldsmith and S. Jin, *Chem. Mater.*, 2017, **29**, 8385–8394.
43 S. Wu, Z. Li, J. Zhang, T. Liu, Z. Zhu and A. K. Jen, *Chem. Commun.*, 2019, **55**, 4315–4318.
44 Y. Fu, M. P. Hautzinger, Z. Luo, F. Wang, D. Pan, M. M. Aristov, I. A. Guzei, A. Pan, X. Zhu and S. Jin, *ACS Cent. Sci.*, 2019, **5**, 1377–1386.